Tribology Letters (2026) 74:124
https://doi.org/10.1007/s11249-026-02221-1

ORIGINAL PAPER

A Strategy for Obtaining Topographically Comparable Tracks Reveals Shifts in Stribeck Curve

Yulong Li[1,2] · **Johannes Schneider**[1,2] · **Christian Greiner**[1,2]

Received: 14 July 2026 / Accepted: 10 October 2026
© The Author(s) 2026

Abstract
Surface topography plays a critical role in the tribological behavior of interacting surfaces. In experimental studies, a controlled variable strategy commonly relies on a limited number of parameters to characterize the state of a surface. However, this approach is intrinsically limited because it reduces multiscale surface morphology to a few descriptors and assumes that the remaining topographic features can be kept comparable. In practice, preparing surfaces that are similar across all length scales is highly challenging. In this study, we established a customized radial grinding strategy to produce circumferential tracks with closely comparable surface topographies at different radial positions on the same 100Cr6 steel disk. The topographic comparability of these tracks was verified across multiple length scales with both roughness parameters and power spectral density (PSD). Lubricated ball-on-disk tests were then performed using 10 mm 100Cr6 steel balls, FVA 1 base oil, a normal load of 2 N, and a multistep sliding speed protocol ranging from 50 mm/s to 600 mm/s. Angle-resolved friction analysis showed that the main spatial distribution of friction was largely preserved among the different radii, although the mean friction level between radii varied systematically with sliding speed. Despite the verified topographic comparability and the similar spatial friction distribution, the resulting Stribeck type curves did not collapse under identical linear sliding speeds. This deviation may arise from differences in angular velocity and/or from multiscale effects of surface topography that are not fully captured by conventional statistical parameters.

Keywords Roughness · Stribeck curve · Surface topography · Sliding radius

1 Introduction

Surface topography is one of the primary boundary conditions in tribological contacts because it influences real contact area [1], local pressure generation [2], asperity interaction [3, 4], lubricant entrainment [5], lubricant storage [6], and wear evolution [7]. In surface preparation, parameters such as R_a and R_q are therefore commonly used as process control and criteria to obtain a desired surface function, with their evaluation relying on standardized parameter definitions, such as those given in ISO 21920–2:2021 [8]. However, surface topography is not merely a specimen descriptor; it is a variable that governs frictional behavior and lubrication state.

Recent topography studies further emphasize that tribological behavior cannot generally be reduced to scalar roughness parameters alone [9]. Although R_a and R_q are useful when the measurement bandwidth and filtering procedure are clearly specified, they cannot capture the full complexity of surface topography. Neglecting the lateral length scale over which roughness is evaluated can lead to substantial disagreement between measurements, whereas scale-dependent descriptors provide a more robust basis for comparing topography data, as shown in a recent multilaboratory surface topography challenge [9]. At the same time, surface orientation [10], anisotropy [7], waviness [11], spectral content [12, 13], and scale-dependent topography may all affect friction and wear [14]. Together, these studies make multiscale surface topography an important consideration in tribology. One particular way to retain this

✉ Yulong Li
yulong.li@kit.edu

✉ Christian Greiner
christian.greiner@kit.edu

[1] Institute for Applied Materials (IAM), Karlsruhe Institute of Technology (KIT), Kaiserstrasse 12, 76131 Karlsruhe, Germany

[2] KIT IAM-ZM MicroTribology Center (μTC), Strasse Am Forum 5, 76131 Karlsruhe, Germany

Published online: 22 October 2026

scale information is the power spectral density (PSD), which decomposes the surface profile into contributions from different wavelengths and therefore links roughness amplitude to lateral length scale rather than compressing the surface into a single scalar value [12, 13].

For experimental tribology, this creates two closely related practical control problems. First, when surface topography itself is the variable of interest, preparing nominally similar surfaces is already challenging, and independently varying a selected topographic scale while keeping the remaining scales unchanged is even more difficult. Second, this lack of topographic reproducibility also affects studies in which another parameter is intended to be isolated. When the influence of load, lubricant, sliding speed, material, texture design, or sliding radius is investigated, the compared experiments should ideally differ only in that single parameter. In practice, however, uncontrollable differences in surface topography may introduce an additional variable. Similar average scalar roughness values are therefore not sufficient; the compared specimens should also be comparable in slope, spacing, orientation, waviness, and multiscale spectral content.

Stribeck curve measurements provide a clear example of this difficulty. Lubricated contacts are commonly interpreted through the Stribeck curve, which relates frictional response to the transition between boundary, mixed, and full film lubrication regimes [5, 15–17]. Because the transition between regimes depends on the relation between lubricant film thickness and surface topography, any uncontrolled difference in surface topography can shift the Stribeck response. This sensitivity is reflected in classical λ type descriptions of mixed lubrication; the corresponding regime boundaries are not universal once asperity interaction, roughness correlation, and surface deformation are considered [4, 18]. In particular, studies on randomly rough lubricated contacts have shown that the mixed to elastohydrodynamic transition is sensitive to how surface roughness is characterized across length scales [19], and that boundary friction reflects the coupled influence of roughness and material properties [20]. Therefore, comparing Stribeck curves across different conditions requires topographic comparability, preferably over multiple length scales, before changes in friction can be confidently attributed to lubrication effects.

Recent studies further reveal why the preparation of comparable surfaces has become an urgent experimental need. Li et al. showed that midscale surface morphology along a sliding track can correlate with friction fluctuations and uneven wear, and that mounting induced tilting or misalignment can introduce systematic changes in friction and wear even under nominally comparable test conditions [21, 22]. Yue et al. likewise examined lubricated pin-on-disk reliability and showed that even a small pin inclination in a self-aligning setup can strongly alter frictional behavior and shift the transition speed between lubrication regimes [23]. These findings amplify the same requirement: if such mechanisms are to be studied systematically, surface topography must first be controlled across the compared experiments. Otherwise, changes attributed to inclination, alignment, kinematics, or lubrication state may still be entangled with residual differences in the surface.

Accordingly, this study makes two closely linked contributions. First, we establish a customized radial grinding strategy for producing circumferential tracks with closely comparable surface topography at different radii on the same disk and verify this comparability using directional profile parameters, PSD-based spectral comparison, and whole track angular surface profiles. Second, using this controlled topography platform, we evaluate Stribeck type curves at different sliding radii, providing a template for experimentally studying the influence of multiscale surface topography.

2 Materials and Methods

2.1 Disk Preparation

The disks were prepared using a customized radial grinding procedure to produce circumferential tracks with comparable surface topographies at different radii. All disks were ground on a cup grinding machine (G&N MPS 2 R300, Erlangen, Germany) equipped with a corundum grinding wheel (grit EK200), using a semi synthetic coolant. As illustrated schematically in Fig. 1a, each disk was mounted concentrically on a rotary table, while the rotating grinding wheel was positioned eccentrically such that its edge passed through the center of the disk. The corresponding grinding kinematics in the top view are shown in Fig. 1b. During grinding, both the grinding wheel and the disk rotated

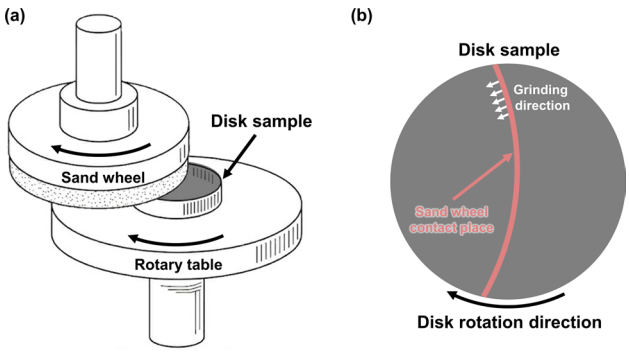


Fig. 1 Schematic illustration of the customized radial grinding strategy used to prepare the disk specimens. **a** Grinding configuration with the disk mounted on a rotary table and the grinding wheel positioned eccentrically. **b** Top view sketch showing how the contact geometry generates a predominantly radial grinding direction on the disk surface

clockwise. Consequently, each point on the disk surface was repeatedly swept by the wheel edge along a nominally radial trajectory. Throughout the grinding process, the rotational speeds of the grinding wheel and the disk were maintained at approximately 2850 rpm and 2 rpm, respectively. The grinding wheel was lowered stepwise by 2 µm after every 1.5 revolutions of the disk, resulting in a total down feed of 20 µm.

2.2 Surface Characterization

Surface topography was characterized by white light interferometry using a TopMap system (Micro.View$^+$, Polytec, Germany). Two topography datasets were used. First, a locally stitched 10× lens topography map was acquired over the 18–24 mm radial band of the disk. In the following, "10× lens dataset" denotes this local high-resolution stitched dataset; it covers approximately 6.0 mm in the radial direction and 0.69 mm along the sliding direction, with a lateral sampling interval of approximately 0.578 µm. This dataset was used to extract the sliding direction profile parameters and local PSDs. Second, a specially configured 0.6× lens developed by Polytec was used for large area topography acquisition. This configuration provided a measurement field of 15.53 mm by 11.71 mm with a calculated lateral optical resolution of 21.35 µm, enabling large area characterization of the whole 70 mm diameter disk while retaining substantial topographic detail.

For a radius-resolved evaluation of the 0.6× lens large area map, the measured surface map was transformed from Cartesian to polar coordinates with respect to the center of the measured area. Annular regions at the target radius positions were extracted using a radial window of ±0.1 mm, corresponding to a total width of 0.2 mm. The angular coordinate was then discretized into 1° bins over the full 0–360° range. Within each annular region, all valid surface height samples whose angular positions fell into the same bin were grouped together, and their arithmetic mean was taken.

For the local surface comparison, four roughness parameters in the sliding direction were extracted from the 10× lens. Namely, the root mean square roughness R_q, reduced valley depth R_{vk}, root mean square slope R_{dq}, and mean spacing of profile elements R_{Sm} were selected to provide complementary information on profile height amplitude, valley characteristics potentially related to lubricant retention, local surface slope, and characteristic lateral feature spacing, respectively. Their names and definitions follow ISO 21920–2:2021 [8]. At each radius, the extracted local field was treated as a stack of line profiles along the sliding direction. The same profile extraction, leveling, and filtering settings were applied to all radii before calculating the profile parameters. Field leveling was applied consistently across all retained profiles.

The surface profiles and their corresponding PSDs were extracted along the local tangential direction at each radial position, ensuring that the profile direction used for the PSD analysis coincided with the actual sliding direction. The PSDs were calculated following the methodology described by Jacobs et al. [10]. The same spectral procedure was applied to both the raw 0.6× lens data and the stitched 10× local topography. For both datasets, sliding direction profiles were extracted at each radius. Each profile was mean removed, Hann windowed, and Fourier transformed. The spatial frequency was converted to wavevector using $q=2\pi f$, after which the spectra were averaged over all valid profiles and logarithmically rebinned for plotting. The PSD from the 0.6× lens, denoted $C_{0.6x}(q)$, gives the low wavevector macroscale roughness contribution, whereas the PSD from the 10× lens provides the small-scale roughness information.

2.3 Tribological Experiments

Tribological tests were carried out in a ball-on-disk configuration using as received 100Cr6 steel balls with a diameter of 10 mm and a surface roughness of $R_q \approx 0.02$ µm. The ball (KGM, Fulda, Germany) and disk (Eisen Schmitt, Karlsruhe, Germany) exhibited comparable hardness values of approximately 800 HV. All experiments were performed on a pin-on-disk tribometer (CSM Instruments, Peseux, Switzerland; now Anton Paar). The test concept is shown schematically in Fig. 2a. The sliding radius was varied by adjusting the extension length of the ball holder cantilever, and the tests were conducted at five radii: 19 mm, 20 mm, 21 mm, 22 mm, and 23 mm. The same disk was used for all five positions, while a fresh ball was employed for each measurement.

Under a normal load of 2 N, Hertzian contact theory gives a contact diameter of 80.4 µm, with mean and maximum contact pressures of approximately 394 and 591 MPa, respectively. FVA 1 base oil (Klueber Lubrication, Munich, Germany), an additive free paraffinic mineral reference oil, was used as the lubricant. Its manufacturer specified kinematic viscosity is 14.5–15.3 mm2/s at 40 °C; the dynamic viscosity was η_0=0.066 Pa·s, measured at 24 °C with a shearing rate of 500 s^{-1}. To obtain Stribeck type data, a stepwise multispeed sequence was applied over nine speed levels between 50 mm/s and 600 mm/s, with a holding time of 2 min at each level, as shown in Fig. 2b. The friction signal was recorded at 10 kHz. To enable a position-resolved friction analysis, the tribometer was retrofitted with a custom zero position trigger. The system consisted of a coaxially mounted metal trigger element fixed to the rotating disk cover and a capacitive sensor arranged in the same horizontal plane. Once per revolution, this assembly defined the angular zero position of the disk, allowing the friction signal to be referenced to a fixed circumferential location. The

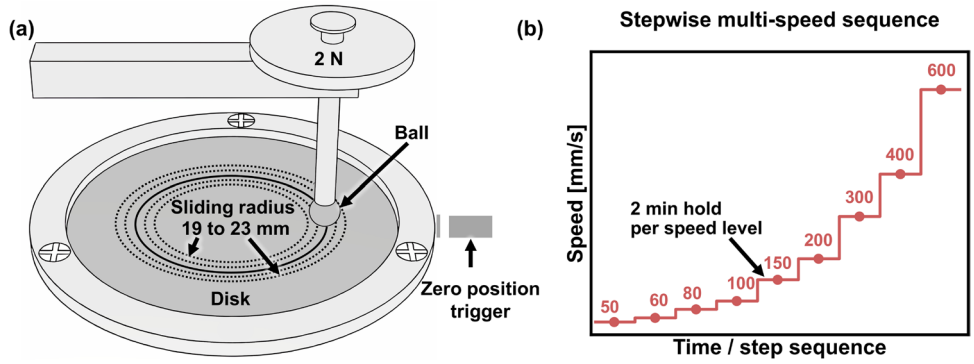


Fig. 2 Schematic representation of the lubricated ball-on-disk test protocol. **a** Test configuration showing the five investigated radii (19–23 mm), the applied normal load, and the custom zero position trigger used to define the angular reference for spatial friction analysis and true speed determination. **b** Stepwise multispeed sequence used in the Stribeck type measurements, with a holding time of 2 min at each speed level

period between consecutive trigger events was additionally used to determine the actual sliding speed of the system.

2.4 Friction Signal Processing

The period between consecutive trigger events was used to determine the experimentally realized rotational response at each speed level. The actual sliding speed was then calculated from the measured rotation period and the corresponding test radius. For angle-resolved friction evaluation, the trigger resets were further used to separate individual revolutions, and the friction data at a given radius and speed level were mapped onto a 1° angular grid over 0–360°. The friction values in each angular bin were then averaged over all revolutions to obtain the phase-averaged angular friction curve $\mu_{r,v}(\theta)$. When Z-score maps or Z-score line plots are shown, $\mu_{r,v}(\theta)$ was standardized as:

$$\overline{\mu}_{r,v} = \frac{1}{N}\sum_{i=1}^{N}\mu_{r,v}(\theta_i) \tag{1}$$

$$s_{\mu,r,v} = \sqrt{\frac{1}{N}\sum_{i=1}^{N}[\mu_{r,v}(\theta_i) - \overline{\mu}_{r,v}]^2} \tag{2}$$

$$Z_{\mu,r,v}(\theta) = \frac{\mu_{r,v}(\theta) - \overline{\mu}_{r,v}}{s_{\mu,r,v}} \tag{3}$$

where N is the number of angular bins in the corresponding friction curve.

2.5 Film Thickness and Multiscale Index

Following the classical film thickness framework introduced by Dowson et al., the entrainment speed was defined as the mean surface speed, $U_e=(u_{ball}+u_{disk})/2$ [18, 24]. Under the present stationary ball and moving disk condition, $u_{ball}=0$ and $u_{disk}=U_{true}$, so that $U_e=U_{true}/2$.

The reference film thickness scale was then estimated with the Hamrock–Dowson point contact relation for the minimum film thickness [24–27]. The dimensionless speed, material, and load parameters were defined as $U=\eta_0 U_e/(E'R)$, $G=\alpha_{pv}E'$, and $W=F_N/(E'R^2)$, respectively. Here, $\eta_0=0.066\ Pa{\cdot}s$ is the measured lubricant dynamic viscosity, U_e is the entrainment speed, α_{pv} is the pressure viscosity coefficient, F_N is the normal load, R is the reduced radius in the entrainment direction, and E' is the reduced modulus given by $1/E'=(1-\nu_{ball}^2)/E_{ball}+(1-\nu_{disk}^2)/E_{disk}$. In the following, h_{ref} denotes minimum reference film thickness; it varies with sliding speed but is taken as identical for all radius at a given speed:

$$h_{ref} = 3.63RU^{0.68}G^{0.49}W^{-0.073}\left(1 - e^{-0.68k}\right) \tag{4}$$

where k is the ellipticity parameter. The Hamrock–Dowson expression was used as a fully flooded reference model, with $R=R_{ball}$ and $k=1$.

The quadratic mean surface roughness was written as:

$$\sigma_{base} = \sqrt{R_{q,ball}^2 + R_{q,10\times}^2} \tag{5}$$

The corresponding lubrication index was then evaluated as [4, 24]:

$$\lambda_{base} = \frac{h_{ref}}{\sigma_{base}} \tag{6}$$

Here, $R_{q,ball}$ was kept constant at 0.02 µm, while $R_{q,10\times}$ denotes the sliding direction profile RMS roughness from the local 10× lens topography at the corresponding radius.

The multiscale index kept the same reference film thickness and modified only the effective roughness in the

denominator. The scale separation was made at the Hertz contact diameter, taken here as 80.4 μm. Since q was defined as the angular wavevector, $q=2\pi/\lambda$, this length gives $q_*=2\pi/(80.4\ \mu m)=0.078\ \mu m^{-1}$.

The 10× lens data were used for surface feature wavelengths smaller than the contact diameter. Following the standard PSD relation in which the integrated spectral density gives the height variance [10], the microscale contribution was extracted from the local 10× lens sliding direction PSD over $q>q_*$:

$$\sigma_{micro} = [\int_{q_*}^{q_{max}} C_{10\times}(q)dq]^{1/2} \tag{7}$$

Here, $q_{max}=\pi/\Delta x=5.44\ \mu m^{-1}$ is the Nyquist limit of the stitched 10× lens topography, using the lateral sampling interval of $\Delta x\approx 0.578\ \mu m$.

The 0.6× lens data were used for surface feature wavelengths larger than the contact diameter. The macroscale contribution was extracted from the raw annulus sliding direction PSD described above, using only the low wavevector band:

$$\sigma_{macro} = [\int_{0<q<q_*} C_{0.6\times}(q)dq]^{1/2} \tag{8}$$

To account for a possible speed dependent change in the relevant topographic scale, we introduced a simple empirical transition. This transition is based on the working hypothesis that the surface scale most relevant to the friction response varies with speed. Specifically, we assume that large-scale height variations dominate at low speed, whereas increasing entrainment speed and stronger hydrodynamic pressure generation progressively shift the relevant contribution toward smaller roughness scales. The speed dependent weight was defined as:

$$w(U_e) = \frac{1}{1+(U_e/U_c)^m} \tag{9}$$

Here, U_e is the entrainment speed, $U_c=186\ mm/s$, and $m=10$. When w is close to one, the 0.6× lens annular roughness dominates; when w decreases, the PSD roughness becomes dominant. The effective disk roughness was then written as:

$$R_{q,eff} = \sqrt{w\sigma_{macro}^2 + (1-w)\sigma_{micro}^2} \tag{10}$$

The total effective composite roughness was:

$$\sigma_{total,eff} = \sqrt{R_{q,ball}^2 + R_{q,eff}^2} \tag{11}$$

The ball roughness contributes only a minor fraction of the total composite roughness and is combined only after the effective disk roughness has been evaluated, consistent with the as received ball surface finish of $R_{q,ball}=0.02\ \mu m$. The corresponding multiscale mixed lubrication index was evaluated as:

$$\lambda_{MS} = \frac{h_{ref}}{\sigma_{total,eff}} \tag{12}$$

2.6 Deviation Metrics

To compare the radius-dependent spread in friction and in scale-resolved topography using the same metric, a normalized mean pairwise deviation was used. For any radius-dependent quantity $x_i(a)$ evaluated at condition a, the deviation was defined as:

$$D_x(a) = \frac{\frac{2}{N_r(N_r-1)}\sum_{i<j}\left|x_i(a)-x_j(a)\right|}{\frac{1}{N_r}\sum_{i=1}^{N_r}x_i(a)} \tag{13}$$

where $N_r=5$ is the number of tested radius positions.

For the friction deviation, a is the sliding speed v and $x_i(a)=\mu_i(v)$, where $\mu_i(v)$ is the mean coefficient of friction at radius i for that speed level. Thus, $D_\mu(v)$ quantifies the relative separation of the Stribeck branches at each speed.

For the PSD-based topography deviation, the PSD was divided into nonoverlapping logarithmic q bands. In each band, the PSD roughness amplitude was calculated as:

$$\sigma_i(q_1,q_2) = [\int_{q_1}^{q_2} C_i(q)dq]^{1/2} \tag{14}$$

where $C_i(q)$ is the sliding direction PSD at radius i and q_1 and q_2 are the lower and upper wavevector limits of the band. In Eq. 13, $a=(q_1,q_2)$ and $x_i(a)=\sigma_i(q_1,q_2)$, giving a dimensionless PSD-based topography deviation for each wavelength band.

3 Results

3.1 Comparable Surface Topography at Different Radii

To verify that the preparation method shown in Fig. 1 produced similar surface topography at different radii, the precontact tracks were first characterized using profile parameters defined in ISO 21920–2:2021 [8]. The extracted local regions from the 10× lens stitched surface topography are shown in Fig. 3a. With the sliding direction oriented from top to bottom, similar grinding grooves were observed at all investigated radius. As shown in Fig. 3b, R_q ranged from 0.31 to 0.33 μm and R_{vk} from 0.24 to 0.27 μm.

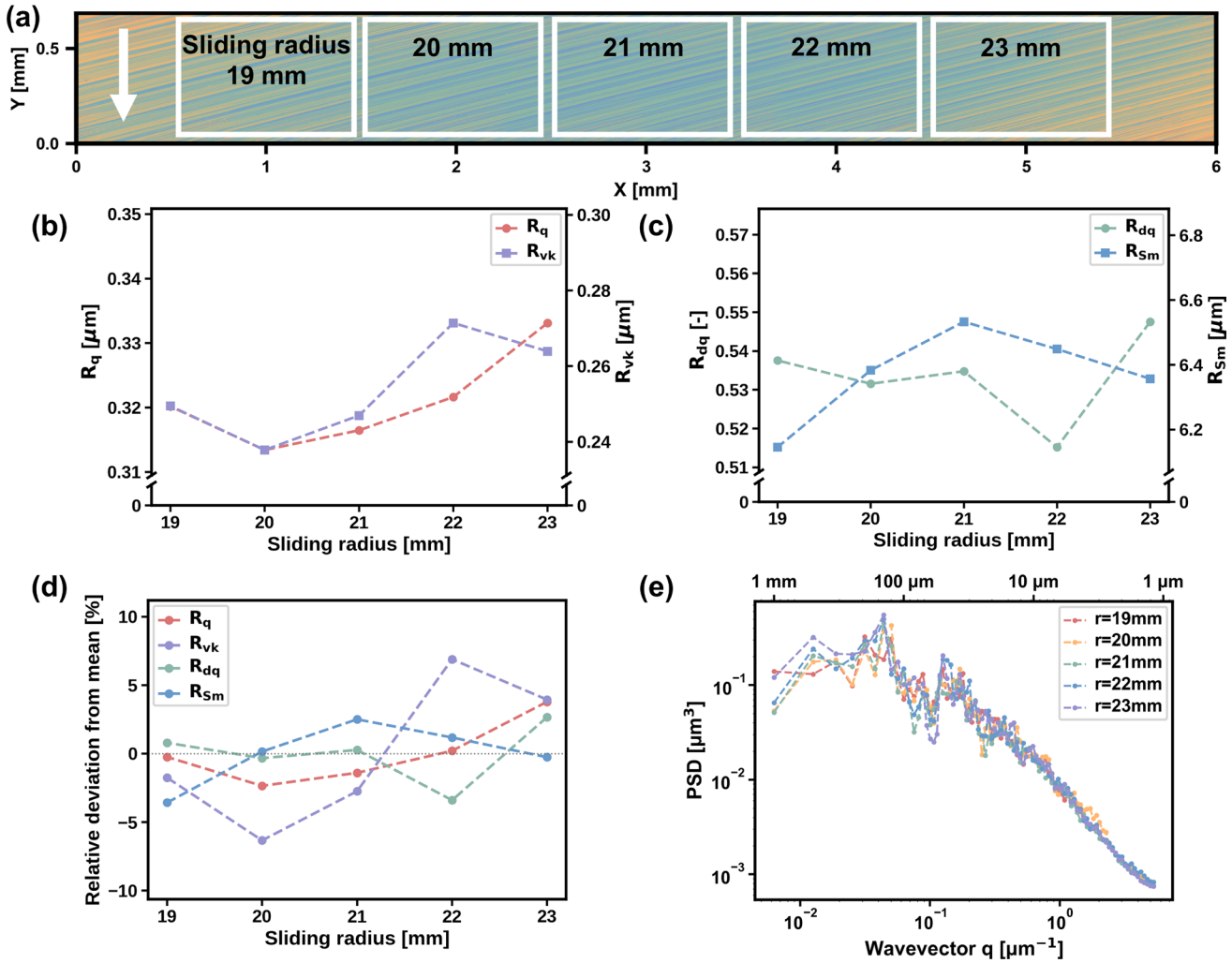


Fig. 3 Local surface topography comparison for the five tested radii. **a** Extracted regions from the 10× lens stitched surface topography, showing the similar sliding direction orientation across the selected tracks. **b** Radius dependence of the profile RMS roughness R_q and reduced valley depth R_{vk} along the sliding direction. **c** Radius dependence of the RMS slope R_{dq} and the mean spacing of profile elements R_{Sm} along the sliding direction. **d** Relative deviation of the profile parameters from their mean values. **e** One-dimensional power spectral density (PSD) curves calculated along the sliding direction for the tracks extracted at different radii in **a**, showing high spectral similarity among the measured tracks. The dashed lines do not imply any functional relationship

Likewise, Fig. 3c shows narrow ranges for both R_{dq}, from 0.52 to 0.55, and R_{Sm}, from 6.15–6.53 µm.

The relative deviation of each surface parameter from its mean value across the five tracks is shown in Fig. 3d. The deviations remained below approximately 6% for R_q, 13% for R_{vk}, 6% for R_{dq}, and 6% for R_{Sm}, without a monotonic trend with sliding radius. One-dimensional power spectral density (PSD) curves calculated along the sliding direction at different radius positions are shown in Fig. 3e. The curves exhibit comparable multiscale spectral content, with only minor differences at low wavevectors and nearly overlapping spectra at medium and high wavevectors. The remaining spectral differences did not show a systematic dependence on radius.

Using the Polytec 0.6× lens, the whole surface topography of the precontact areas at different radii is shown in Fig. 4. The top view of selected radius is shown in Fig. 4a, while the optical microscope image in Fig. 4b illustrates the nearly constant contact angle between the circumferential sliding direction and the radial grinding grooves across different radii. The raw angular surface profiles in Fig. 4c show that all five tested radii exhibited similar profiles. Broad maxima appeared around approximately 100°–130° and 290°–320°, while a pronounced minimum occurred near 220°–240°. A sharp drop around 200° was also visible in all profiles. After normalization by the initial angular position, shown in Fig. 4d, the overlap among the profiles became clearer. Along each wear track at different radii, the

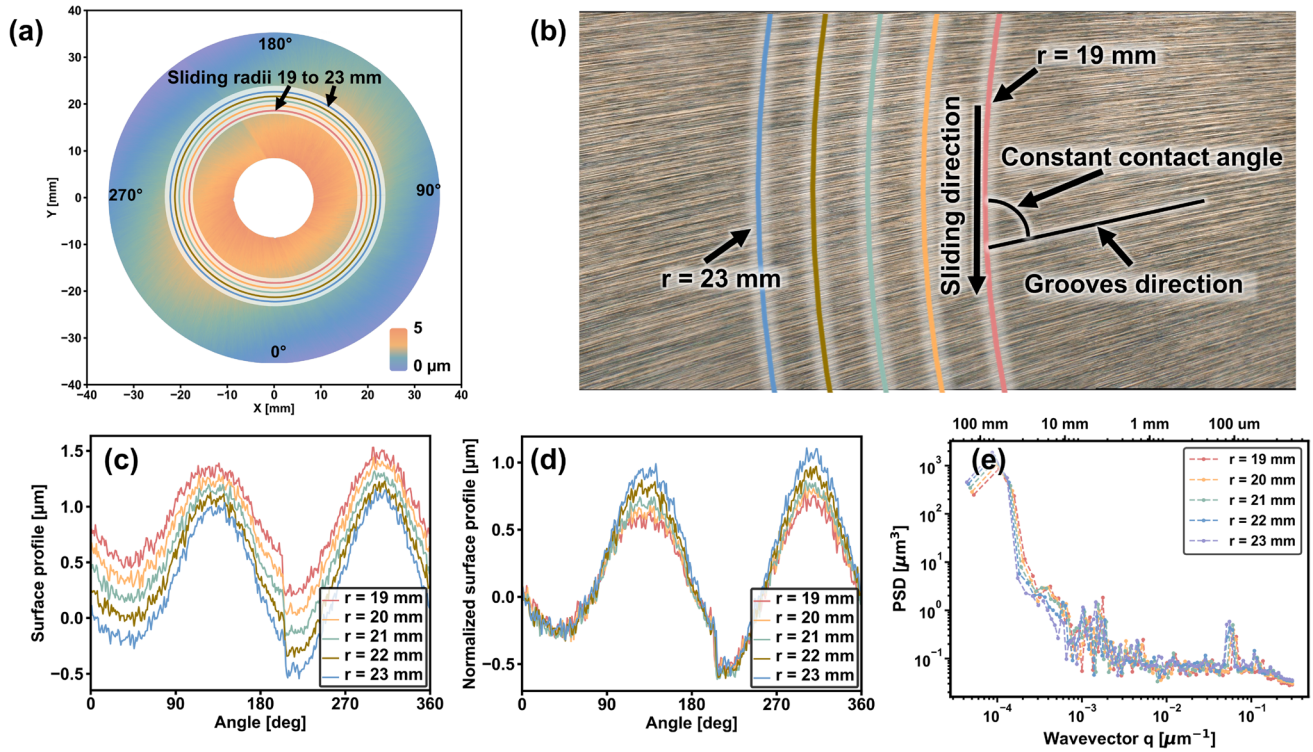


Fig. 4 The whole surface topography of the precontact areas at different radii. **a** Top view of surface topography with the selected annular tracks between 19 and 23 mm. **b** Optical microscope image illustrating the nearly constant contact angle between the circumferential sliding direction and the radial grinding grooves. **c** Angular surface profiles. **d** Profiles normalized by the initial angular position. **e** One-dimensional power spectral density (PSD) curves calculated from the Polytec 0.6× lens data in **a**. Annular regions at the target radii were extracted using a radial window of ±0.1 mm, corresponding to a total width of 0.2 mm. The PSD was calculated directly from the raw lens points

maximum height variation, over an average circumference of 132 mm, was below 0.4 µm. The power spectral density (PSD) curves were calculated from the Polytec 0.6× lens raw data in Fig. 4a. Annular regions at the target radii were extracted using a radial window of ±0.1 mm, corresponding to a total width of 0.2 mm. The PSD was calculated directly from the raw annulus points. The spectra remained broadly comparable across the five radii, with the largest visible differences concentrated at the lowest wavevectors and much closer overlap at intermediate and higher wavevectors.

3.2 Stribeck type Curves

After the topographic comparability of the selected tracks had been established, the disk in Fig. 4 was used to test whether constant sliding speed produces equivalent frictional behavior at different radii. The linear speed was kept as consistent as possible by controlling the angular velocity. As shown in Fig. 5a, the experimentally realized linear speeds at the different radii were very close at each speed step. In Fig. 5a, the five datasets do not collapse onto a single curve at constant sliding speed; instead, they form a family of systematically shifted branches. The separation is most pronounced between approximately 50 mm/s and 200 mm/s. The tracks at larger radius, especially r=22 mm and r=23 mm, generally occupy the upper part of the family.

Figure 5b replots the same measurements shown in Fig. 5a, but with the horizontal axis changed from linear speed to angular velocity. The five curves at different radii in Fig. 5b become more closely grouped than in the sliding speed representation in Fig. 5a. This convergence is most evident at intermediate and high angular velocities, where the separation between the curves is reduced. At lower angular velocities, the curves remain more clearly separated, with the larger radius tracks still generally located toward the upper part of the dataset.

Figure 5c shows the classical lambda ratio representation based on λ_{base}, calculated from the Hamrock–Dowson minimum film thickness [25, 26] and the 10× lens profile roughness $R_{q,10\times}$ along the sliding direction. For the present test conditions, the reference film thickness ranged from about 16 nm at 50 mm/s to about 86 nm at 600 mm/s. Compared with Fig. 5a, the curves in Fig. 5c show only a modest increase in grouping and no pronounced change in their overall arrangement. The five radii-dependent curves remain distinguishable, with the largest spread at low λ_{base}

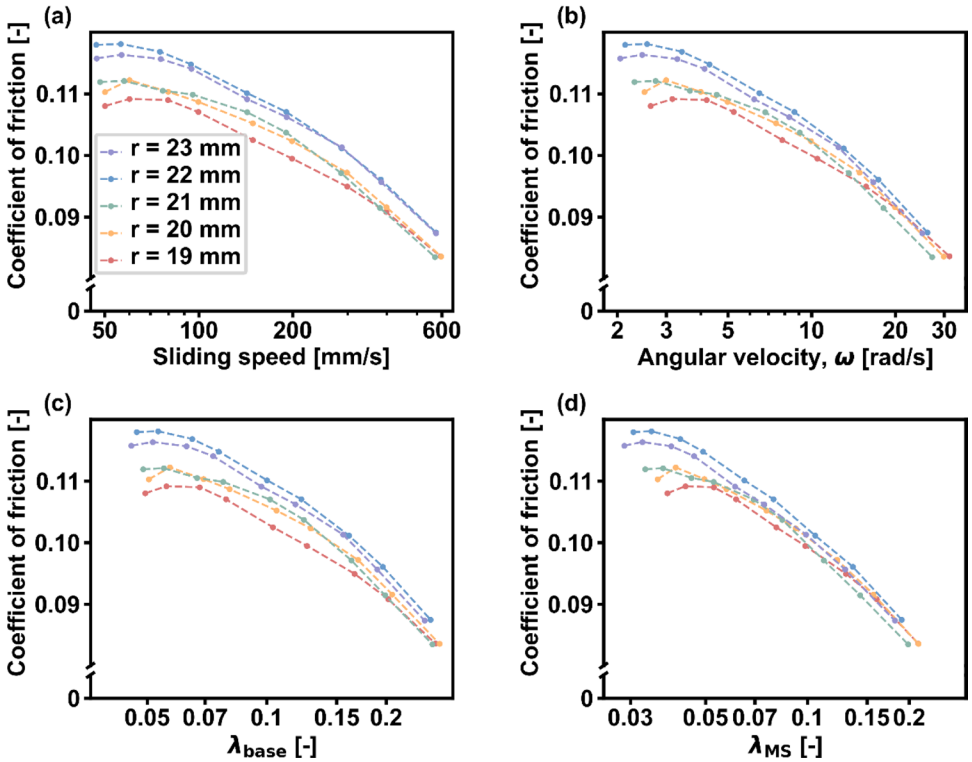


Fig. 5 Stribeck type curves at different radii. **a** Coefficient of friction plotted against the measured true sliding speed. **b** Coefficient of friction plotted against the measured angular velocity. **c** Coefficient of friction plotted against the baseline mixed lubrication index λ_{base} based on the Hamrock [25, 26] minimum film thickness and the 10× lens profile roughness $R_{q,10\times}$ along the sliding direction. **d** Coefficient of friction plotted against the topography multiscale lubrication index λ_{MS} proposed in this work. In this index, large-scale, low wavevector surface topography dominates at low and medium speeds, while small-scale, high wavevector surface topography dominates at high speeds

and closer grouping toward higher λ_{base}. Figure 5d plots the same coefficient of friction data against the topography multiscale lubrication index λ_{MS}, calculated according to Eq. 12. Among the four representations in Fig. 5a-(d), this representation gives the closest grouping of the five radii-specific branches. A residual separation is still visible at the lowest λ_{MS} values, but the branch spacing is smaller than in the sliding speed, angular velocity, and baseline λ_{base} representations. Quantitatively, the overall RMSE (root mean square error) of the five radii-specific datasets relative to a pooled reference fit is 1.95×10^{-3} for λ_{MS}, compared with 2.57×10^{-3} for λ_{base}.

3.3 Spatially Resolved Friction

Figure 6a shows the angle-resolved friction curves at a representative radius of 21 mm. The absolute friction level decreases with increasing sliding speed, while the overall spatial friction trend remains similar. Across the different sliding speeds, friction rises from the initial region to a broad maximum around 90°–180°, decreases to a lower friction region around 240°–320°, and then increases again toward the end of the cycle.

This persistence becomes more apparent in the friction Z-score representation in Fig. 6b. The Z-score quantifies how strongly a local friction value deviates from the disk averaged value relative to the overall data spread (defined in Eq. 3). After removal of the mean friction level at each speed, the same positive and negative angular sectors remain visible over nearly the entire speed range. The spatial friction Z-score maps in Fig. 6(c,d) show that this behavior is retained at different radii, here exemplified by 21 mm and 22 mm (see Figure S1for 19 mm, 20 mm and 23 mm). A positive band remains concentrated mainly between about 90° and 180°, indicating a tendency toward higher friction across different sliding speeds, whereas at around 240°–320° remains predominantly negative and corresponds to consistently lower friction.

To verify whether the similarity of the spatial friction distribution across different radius persists at both low and high sliding speeds, two representative speeds were selected: 60 mm/s in Fig. 7(a) and 200 mm/s in Fig. 7b. At both speeds, the friction curves retain nearly the same spatial distribution, while showing a clear separation in absolute friction value. The tracks at larger radius generally lie above those at smaller radius, especially at the lower speed, but the locations of the main high and low friction regions remain aligned. The spatial friction Z-score maps in Fig. 7(c,d) show that changing radius mainly affects the mean level and amplitude of friction, rather than reorganizing the spatial distribution.

Figure 8 provides a more direct comparison between the spatial friction distribution and the precontact surface topography at a sliding radius of 21 mm. At each investigated sliding radius, higher friction occurs mainly between 90° and 180°, which coincides with an approximately 2 µm

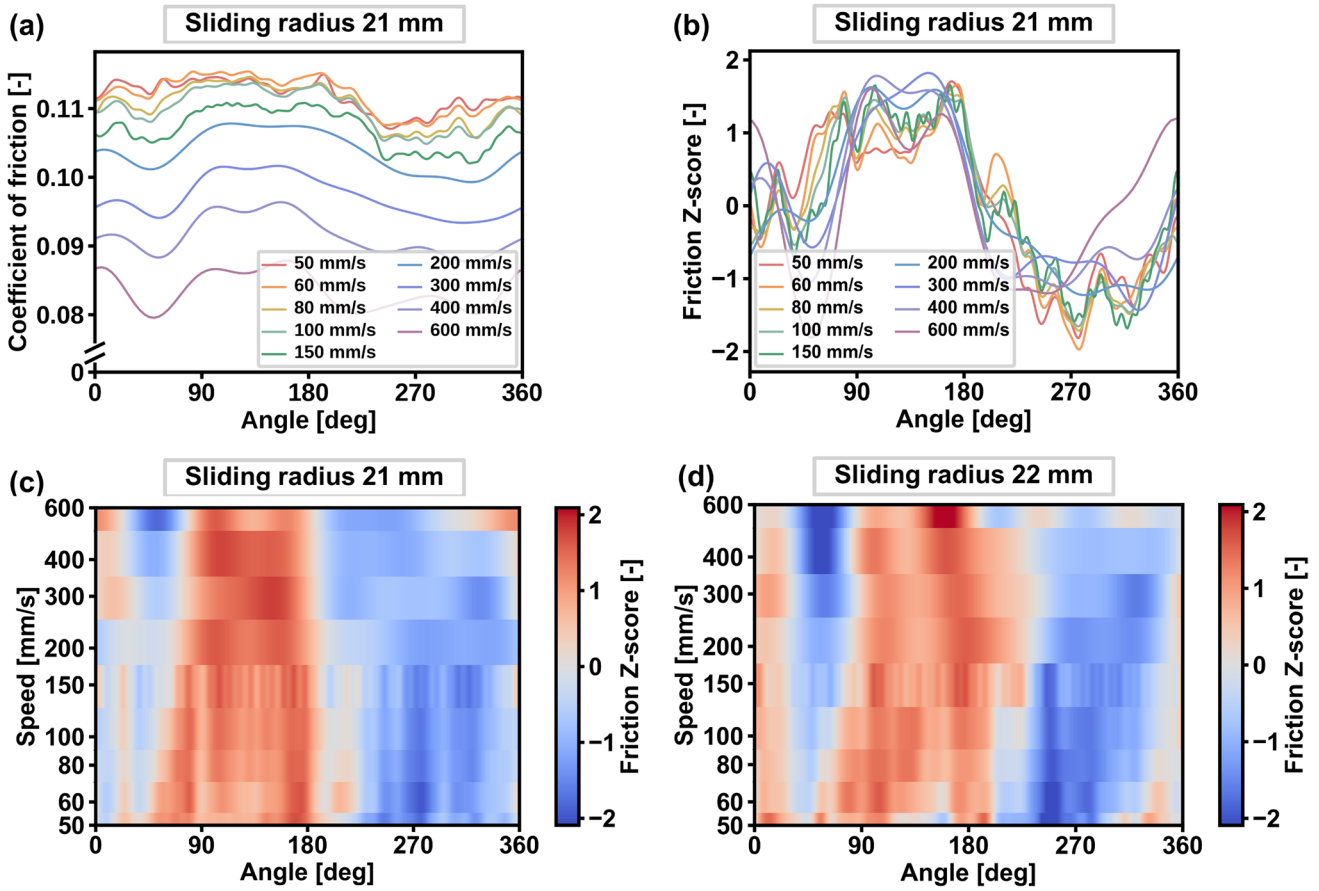


Fig. 6 Angle-resolved friction evolution with sliding speed. **a** Coefficient of friction as a function of angular position at 21 mm. **b** Corresponding friction Z-score profiles at the same radius. **c**,**d** Spatial friction Z-score maps at 21 mm and 22 mm (Spatial friction Z-score maps for 19 mm, 20 mm, and 23 mm radii are in Figure S1), respectively

protrusion in the whole track surface topography over the 132 mm circumferential track. In contrast, the topographic peak around 300° does not correspond to a similarly high friction region.

3.4 Friction and Surface Topography Deviation

Figure 9 summarizes the radius to radius difference in friction and in PSD-based surface roughness. The friction deviation in Fig. 9a was calculated by comparing the mean coefficient of friction of the five radii at each sliding speed. The plotted friction deviation therefore describes the absolute mean pairwise branch separation among the five radii at the same speed. It decreases from about 5.1×10^{-3} at 50 mm/s to about 2.4×10^{-3} at 600 mm/s, showing that the radius-dependent branch separation becomes smaller at higher sliding speed.

The PSD-based topography deviation in Fig. 9b describes the relative radius to radius difference in surface topography at a given wavevector band. For each radius, $\sigma_i(q_1,q_2)$ was first obtained from Eq. 14 by integrating the PSD over the corresponding wavevector band; this gives the RMS roughness amplitude within that scale range. The five radii values were then compared with Eq. 13. The PSD-based deviation is the largest in the low wavevector range. It reaches approximately 0.28–0.30 around $q\approx4\times10^{-4}$ μm^{-1} and then decreases with increasing wavevector to about 0.10 near $q\approx10^{-2}$ μm^{-1}. At higher wavevectors, from approximately $q=10^{-1}$ μm^{-1} to $q=1$ μm^{-1}, the deviation fluctuates mostly between 0 and 0.10, with several local peaks around 0.08–0.11. This indicates that the residual topographic differences between tracks are most pronounced at the larger surface scales, while the shorter-wavelength roughness is more comparable but not completely identical.

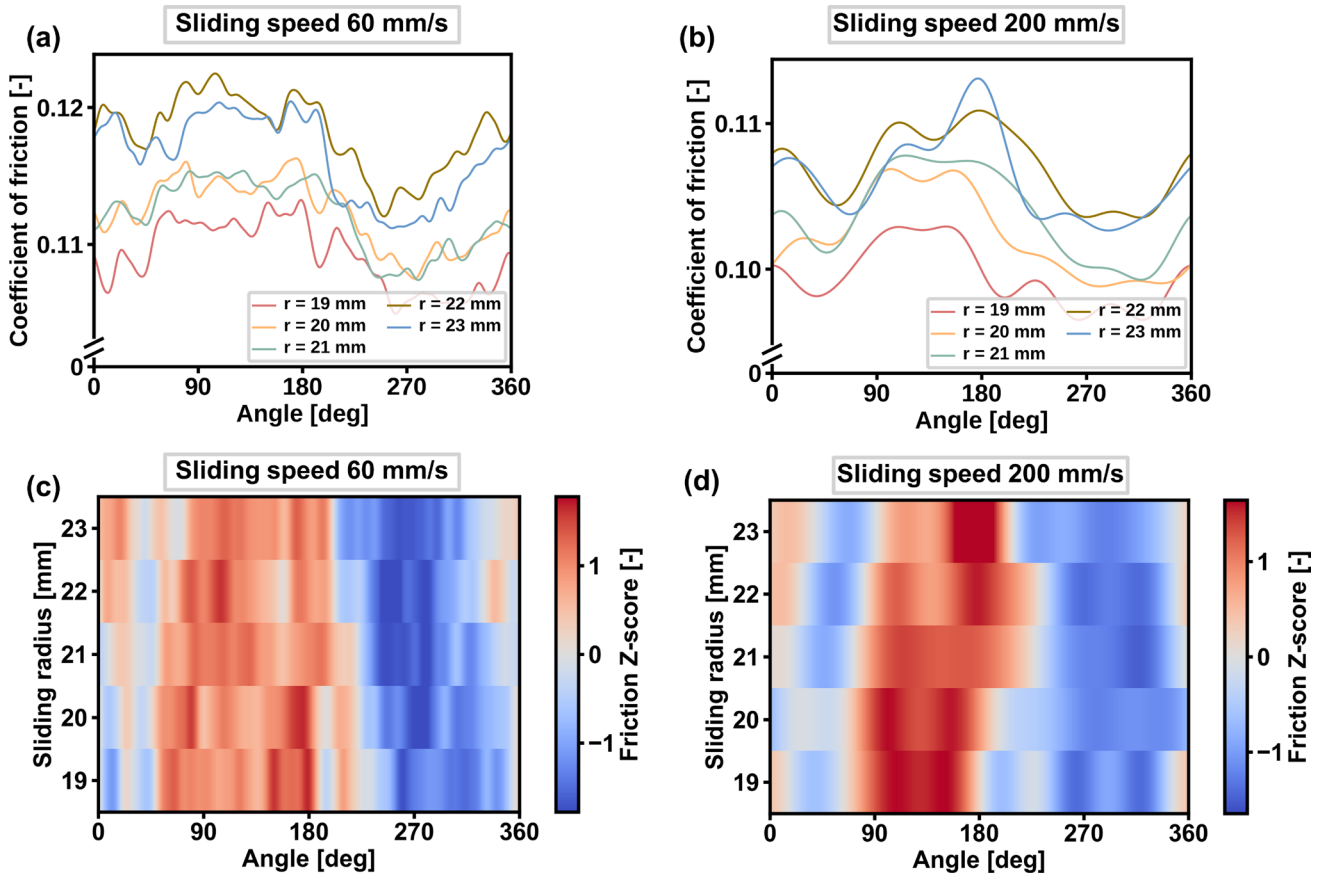


Fig. 7 Spatial friction at five radii under two representative sliding speeds. **a**,**b** Coefficient of friction versus angular position at 60 mm/s and 200 mm/s. **c**,**d** Spatial friction Z-score maps at the same two speeds and five radii

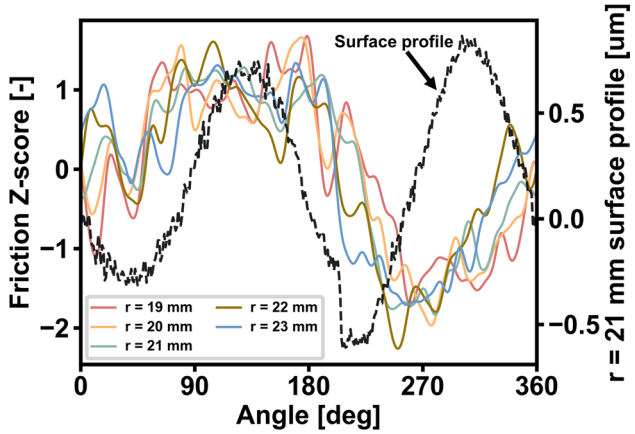


Fig. 8 Spatial friction at different radii compared with whole track surface topography at 60 mm/s. The friction curves for the five radii are independently standardized using the Z-score to remove mean branch offsets. The dashed black curve shows the normalized 0.6× annular surface profile at 21 mm on the right axis

4 Discussion

4.1 Topographical Comparability of the Prepared Tracks

A central requirement for comparing Stribeck type responses under different conditions is that surface topography should not act as an uncontrolled hidden variable. In the present work, the customized radial grinding strategy produced circumferential tracks with a high degree of statistical and spectral comparability. As shown in Fig. 3, the local profile parameters varied only within narrow ranges across the five investigated radii: R_q ranged from 0.31 to 0.33 µm, R_{vk} ranged from 0.24 to 0.27 µm, R_{dq} ranged from 0.52 to 0.55, and R_{Sm} ranged from 6.15 to 6.53 µm. Their relative deviations from the mean remained below approximately 6% for R_q, 13% for R_{vk}, 6% for R_{dq}, and 6% for R_{Sm}. Moreover, Fig. 3a shows that the texture orientation was also highly similar for all tracks. In addition, the one-dimensional PSD curves along the sliding direction in Fig. 4a largely overlapped at medium and high wavevectors, with only minor residual differences at the lowest wavevectors. Thus, the

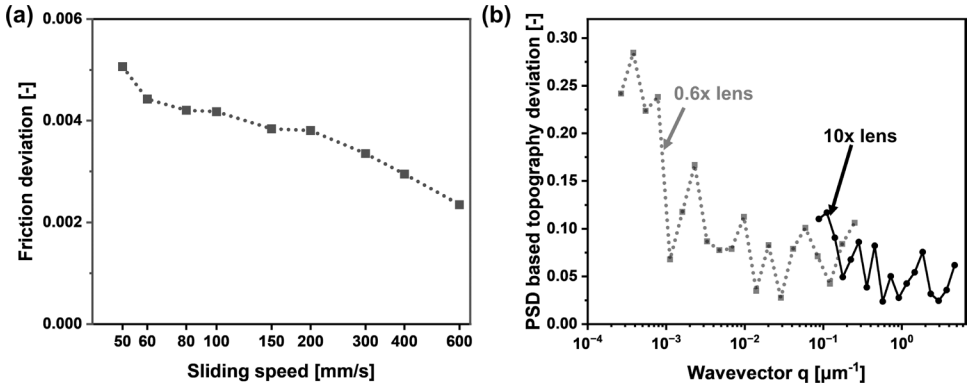


Fig. 9 Radius to radius friction deviation and PSD-based topography deviation. **a** Mean friction deviation among the five radii as a function of sliding speed. **b** PSD-based topography deviation as a function of wavevector q, obtained from band integrated roughness amplitudes; the 0.6× lens data (gray) capture the larger-scale topography, while the 10× lens data (black) capture the shorter-wavelength local roughness

selected tracks were comparable not only in terms of a single scalar roughness value, but also with respect to amplitude, slope, spacing, texture orientation, and multiscale spectral content. The orientation of the grooves relative to the sliding direction was also the same for all tracks at the same angular position (Fig. 4b), so directional topography did not differ between tracks.

This level of agreement is essential because surface functionality cannot generally be reduced to scalar roughness values such as R_a or R_q; scale-dependent topographic features can influence lubricant entrainment, asperity interaction, and local pressure generation [1, 3, 9–12, 14, 28]. The combined agreement in conventional profile parameters, texture orientation, and PSD-based descriptors demonstrates that the present preparation route produced surfaces with strong multiscale topographic similarity, thereby providing not only a more reliable benchmark for Stribeck curve measurements under different conditions, but also a solid experimental basis for probing the multiscale effects of roughness on friction.

4.2 Surface Topography and Spatial Friction Distribution

The spatially resolved friction results in Figs. 6 and 7 show that the topographic comparability achieved by the preparation route is reflected in the friction response. At both representative sliding speeds in Fig. 7(a,b), the friction curves measured at different radii exhibited different absolute friction levels, but retained a similar angular distribution. After Z-score normalization in Fig. 6(b-d) and Fig. 7(c,d), this similarity becomes even clearer: the main friction maxima and minima remained spatially aligned across different radii and sliding speeds. Thus, changes in sliding radius and sliding speed change the absolute friction level and the amplitude of the angular variation, but did not reorganize the spatial friction distribution itself. In other words, the prepared tracks generated comparable spatial friction patterns, even though their absolute friction values were not identical.

In Fig. 8, the main high friction region appears predominantly between approximately 90° and 180°, where the whole track surface topography contains an approximately 2 µm protrusion over the 132 mm circumferential track. Such a sensitivity is consistent with previous findings showing that waviness features along a sliding track can substantially alter local friction and wear [21]. However, the topographic peak around 300° in Fig. 8 does not generate an equally pronounced high friction region. The spatial friction distribution is therefore not a point-to-point mapping of local height. Instead, the spatial friction distribution most likely results from a coupled response involving large-scale surface topography, local curvature, lubricant entrainment, transient squeeze film effects, and contact mechanics. Recent work on friction prediction across different lubrication conditions likewise emphasizes that friction cannot be assigned to a single roughness parameter alone, but depends on how the surface and lubrication state interact [22]. The present results are therefore consistent with the view that large-scale surface topography provides a spatial template for friction, while the final friction response and the absolute friction value are determined by the coupled tribological system.

Consequently, the ability to create topographically comparable tracks provides a controlled baseline for tribological testing, allowing friction responses at different radii and speeds to be compared without conflating absolute friction changes with changes in spatial friction distribution. This makes the approach useful for Stribeck curve measurements, lubricant or additive comparisons, and studies of replenishment, running in, and wear evolution, because the initial surface topography can be treated as a controlled experimental variable rather than an uncontrolled source of scatter.

4.3 Stribeck Shifts

Despite topographic comparability, the Stribeck type curves did not collapse into a single branch when plotted against constant sliding speed in Fig. 5a. Instead, the five radius-dependent datasets formed systematically shifted branches, with the separation most pronounced between approximately

50 mm/s and 200 mm/s. This result shows that constant sliding speed alone is not sufficient to guarantee equivalent lubrication conditions in rotational sliding. A similar radius dependence under constant linear speed was observed by Grützmacher et al., who found that larger sliding radius led to a substantially longer oil film lifetime in rotational sliding and attributed this to reduced centrifugal removal of lubricant at lower angular velocity [29].

When the same data were replotted against angular velocity in Fig. 5b, the branches became more closely grouped, especially at intermediate and high angular velocities. This suggests that angular velocity, and the associated lubricant redistribution, replenishment, and centrifugal transport, may contribute to the observed branch separation. Such an interpretation is physically plausible because rotational sliding introduces lubricant transport processes that are not fully captured by sliding speed alone. Lubricant replenishment can also strongly affect starved contacts because the available lubricant near the inlet depends on how quickly lubricant returns to the contact track [30, 31].

A classical λ representation based on the Hamrock–Dowson film thickness scale only modestly improved the grouping in Fig. 5c [25, 26]. This may be because the single local roughness scale used in Eqs. (5) and (6) does not capture the multiscale influence of surface topography. The trends in Fig. 9 therefore motivated the scale-dependent topography hypothesis introduced in Eq. 12. In Fig. 9a, the friction deviation among the five radii decreased from about 5.1×10^{-3} at 50 mm/s to about 2.4×10^{-3} at 600 mm/s. Meanwhile, the dimensionless PSD-based topography deviation in Fig. 9b was the largest at low wavevectors, reaching approximately 0.28–0.30 around $q\approx4\times10^{-4}$ μm^{-1}, then decreasing to about 0.10 near $q\approx10^{-2}$ μm^{-1} and fluctuating mostly below 0.10 at higher wavevectors. The friction deviation is thus largest at the lowest speeds, and the topography deviation is largest at the largest scales. Laser surface texturing studies have likewise shown that the dimple diameter most effective in reducing friction depends on the local velocity gradient rather than on a single fixed optimum [32]. We therefore hypothesize that the surface scale most relevant to friction varies with operating conditions: large-scale surface components may dominate under thin film conditions, and their influence diminishes as the hydrodynamic film builds up. This scale-dependent picture is also consistent with multiscale contact mechanics theory, in which the length scales that carry the contact depend on the resolution at which the interface is examined [33, 34].

Based on this hypothesis, we introduce the topography multiscale lubrication index λ_{MS}. The measured friction deviations in Fig. 9a are compared directly with the topography deviations in Fig. 9b to estimate the characteristic topographic scale associated with the residual branch separation at each sliding speed. This follows a similar reasoning to the reversed comparison for rough anisotropic contacts, where the active film controlling scale is inferred from friction rather than imposed through a predefined λ criterion [19]. With λ_{MS}, the five branches group more closely in Fig. 5d; the RMSE relative to the pooled reference fit is approximately 24% lower than for the classical λ representation.

Although the present preparation route minimized topographic differences between sliding radii, residual differences still remained at certain length scales. Because these multiscale topographic differences and the radius-dependent angular velocity changes coexist, their individual contributions cannot be uniquely separated here. Further studies, for example, with independent film thickness measurements and direct characterization of lubricant supply near the inlet, would be needed to distinguish changes in film formation from changes in the effective roughness scale. In this sense, λ_{MS} should be read as an empirical organizing parameter and as an experimental attempt to incorporate multiscale topographic considerations into lubricated friction analysis, highlighting the need to move beyond single parameter roughness descriptions in tribology [4, 9, 35, 36].

5 Conclusion

In this contribution, we proposed a radial grinding-based preparation strategy to produce circumferential tracks with closely comparable surface topography at different radii. The prepared tracks showed strong similarity not only in conventional profile parameters, but also in texture orientation and PSD-based multiscale spectral characteristics. The spatially resolved friction measurements further confirmed the effectiveness of this controlled topography. Although the absolute friction level varied with sliding radius and speed, the normalized angular friction distribution remained broadly consistent, indicating that the tracks generated comparable spatial friction templates.

Despite this topographic comparability and similar spatial friction distribution, the Stribeck type curves did not collapse under constant linear sliding speed. By considering angular velocity and an assumed multiscale roughness response, the Stribeck type curves obtained at different sliding radius could be organized more consistently. Therefore, the proposed approach provides a controlled basis for comparing lubricated friction responses and also offers an experimental route to investigate multiscale topographic effects in tribological systems. Building on the controlled topography platform established here, future work can more clearly separate the influence of other factors, such as load, lubricant, additives, or speed, on friction and wear, because surface topography no longer acts as an uncontrolled hidden variable. At the same time, the controlled surfaces themselves

already offer an experimental route to probe how multiscale topography affects tribological behavior.

Acknowledgements CG acknowledges the financial support provided by the German Research Foundation through grant (GR 4174/12) as well as funding through a Future Fields grant from Karlsruhe Institute of Technology (KIT).

Author contribution Yulong Li: Conceptualization, Methodology, Investigation, Data curation, Formal analysis, Visualization, Writing—original draft, Writing—review and editing. Johannes Schneider: Methodology, Supervision. Christian Greiner: Conceptualization, Supervision, Funding acquisition, Writing—review and editing.

Funding Open Access funding enabled and organized by Projekt DEAL. Deutsche Forschungsgemeinschaft,GR 4174/12

Data availability The raw data, along with the code used for the evaluation, are published on KITopen (https://doi.org/10.35097/ztmkvseryzt1wabf).

Declarations

Conflict of interest The authors declare no competing interests.

Open Access This article is licensed under a Creative Commons Attribution 4.0 International License, which permits use, sharing, adaptation, distribution and reproduction in any medium or format, as long as you give appropriate credit to the original author(s) and the source, provide a link to the Creative Commons licence, and indicate if changes were made. The images or other third party material in this article are included in the article's Creative Commons licence, unless indicated otherwise in a credit line to the material. If material is not included in the article's Creative Commons licence and your intended use is not permitted by statutory regulation or exceeds the permitted use, you will need to obtain permission directly from the copyright holder. To view a copy of this licence, visit http://creativecommons.org/licenses/by/4.0/.

References

1. Patir, N., Cheng, H.S.: An average flow model for determining effects of three-dimensional roughness on partial hydrodynamic lubrication. J. Lubr. Technol. **100**(1), 12–17 (1978). https://doi.org/10.1115/1.3453103
2. Gropper, D., Wang, L., Harvey, T.J.: Hydrodynamic lubrication of textured surfaces: a review of modeling techniques and key findings. Tribol. Int. **94**, 509–529 (2016). https://doi.org/10.1016/j.triboint.2015.10.009
3. Patir, N., Cheng, H.S.: Application of average flow model to lubrication between rough sliding surfaces. J. Lubr. Technol. **101**(2), 220–229 (1979). https://doi.org/10.1115/1.3453329
4. Zhu, D., Wang, Q.J.: On the λ ratio range of mixed lubrication. Proc. Inst. Mech. Eng. J J. Eng. Tribol. **226**(12), 1010–1022 (2012). https://doi.org/10.1177/1350650112461867
5. Spikes, H.A.: Mixed lubrication—an overview. Lubr. Sci. **9**(3), 221–253 (1997). https://doi.org/10.1002/ls.3010090302
6. Gachot, C., Rosenkranz, A., Hsu, S.M., Costa, H.L.: A critical assessment of surface texturing for friction and wear improvement. Wear **372**, 21–41 (2017). https://doi.org/10.1016/j.wear.2016.11.020
7. Holmberg, K., Laukkanen, A., Hakala, T., Ronkainen, H., Suhonen, T., Wolski, M., Podsiadlo, P., Woloszynski, T., Stachowiak, G., Gachot, C., Li, L.: Topography orientation effects on friction and wear in sliding dlc and steel contacts, part 3: experiments under dry and lubricated conditions. Wear **486**, 204093 (2021). https://doi.org/10.1016/j.wear.2021.204093
8. International Organization for Standardization. Iso 21920–2:2021 geometrical product specifications (gps) — surface texture: Profile — part 2: Terms, definitions and surface texture parameters, 2021. URL https://www.iso.org/standard/72226.html. International Standard.
9. Pradhan, A., Müser, M.H., et al.: The surface-topography challenge: a multi-laboratory benchmark study to advance the characterization of topography. Tribol. Lett. **73**(3), 110 (2025). https://doi.org/10.1007/s11249-025-02014-y
10. Jacobs, T.D.B., Junge, T., Pastewka, L.: Quantitative characterization of surface topography using spectral analysis. Surf. Topogr. Metrol. Prop. **5**(1), 013001 (2017). https://doi.org/10.1088/2051-672X/aa51f8
11. Wang, Y., Li, C., Du, J., Morina, A.: Understanding the influences of multiscale waviness on the elastohydrodynamic lubrication performance, part I: the full-film condition. Lubricants **10**(12), 368 (2022). https://doi.org/10.3390/lubricants10120368
12. Prajapati, D.K., Björling, M.: The influence of non-gaussian roughness and spectral properties on mixed lubrication for heavily loaded counterformal contacts. Lubricants **12**(3), 71 (2024). https://doi.org/10.3390/lubricants12030071
13. Morales-Espejel, G.E.: Surface roughness effects in elastohydrodynamic lubrication: a review with contributions. Proc. Inst. Mech. Eng. J J. Eng. Tribol. **228**(11), 1217–1242 (2014). https://doi.org/10.1177/1350650113513572
14. Wang, Y., Liu, Y.: Understanding the influences of multiscale waviness on the elastohydrodynamic lubrication performance, part II: the partial-film condition. Lubricants **12**(6), 190 (2024)
15. Richard Stribeck. Die wesentlichen eigenschaften der gleit- und rollenlager. Zeitschrift des Vereines Deutscher Ingenieure, 46, 1902. Published in multiple parts, including pp. 1341–1348, 1432–1438, and 1463–1470
16. Hsu, S.M., Gates, R.S.: Boundary lubricating films: formation and lubrication mechanism. Tribol. Int. **38**(3), 305–312 (2005). https://doi.org/10.1016/j.triboint.2004.08.021
17. Spikes, H.A.: Sixty years of EHL. Lubr. Sci. **18**(4), 265–291 (2006). https://doi.org/10.1002/ls.23
18. Hamrock, B.J., Dowson, D.: Elastohydrodynamic lubrication of elliptical contacts for materials of low elastic modulus, I—fully flooded conjunction. J. Lubr. Technol. **100**(2), 236–245 (1978). https://doi.org/10.1115/1.3453152
19. Bonaventure, J., Cayer-Barrioz, J., Mazuyer, D.: Transition between mixed lubrication and elastohydrodynamic lubrication with randomly rough surfaces. Tribol. Lett. **64**(3), 44 (2016). https://doi.org/10.1007/s11249-016-0773-9
20. Bonaventure, J., Cayer-Barrioz, J., Mazuyer, D.: Surface effects on boundary friction with additive-free lubricating films: coupled influence of roughness and material properties. Tribol. Lett. **66**(3), 84 (2018). https://doi.org/10.1007/s11249-018-1030-1
21. Li, Y., Garabedian, N., Schneider, J., Greiner, C.: Waviness affects friction and abrasive wear. Tribol. Lett. **71**(2), 64 (2023). https://doi.org/10.1007/s11249-023-01736-1
22. Li, Y., Gumbsch, P., Greiner, C.: Predicting friction under vastly different lubrication scenarios. Phys. Rev. Res. **8**(2), 023068 (2026). https://doi.org/10.1103/bx4g-8647
23. Yue, H., Schneider, J., Frohnapfel, B., Gumbsch, P.: The influence of pin inclination on frictional behaviour in pin-on-disc sliding and its implications for test reliability. Tribol. Int. **200**, 110083 (2024). https://doi.org/10.1016/j.triboint.2024.110083
24. Marian, M., Bartz, M., Wartzack, S., Rosenkranz, A.: Non-dimensional groups, film thickness equations and correction factors for elastohydrodynamic lubrication: A review. Lubricants **8**(10), 95 (2020). https://doi.org/10.3390/lubricants8100095

25. Hamrock, B.J., Dowson, D.: Isothermal elastohydrodynamic lubrication of point contacts: part III—fully flooded results. J. Lubr. Technol. **99**(2), 264–275 (1977). https://doi.org/10.1115/1.3453074
26. J. Bernard, Hamrock and Duncan Dowson. Film thickness for different regimes of fluid-film lubrication. Technical Report NASA-TM-81700, NASA Lewis Research Center, 1983. URL https://ntrs.nasa.gov/citations/19830020178.
27. Lubrecht, A.A., Venner, C.H., Colin, F.: Film thickness calculation in elasto-hydrodynamic lubricated line and elliptical contacts: the Dowson, Higginson, Hamrock contribution. Proc. Inst. Mech. Eng. J J. Eng. Tribol. **223**(3), 511–515 (2009). https://doi.org/10.1243/13506501JET508
28. Tønder, K.: Hydrodynamic effects of tailored inlet roughnesses: extended theory. Tribol. Int. **37**(2), 137–142 (2004). https://doi.org/10.1016/S0301-679X(03)00043-4
29. Grützmacher, P.G., Rosenkranz, A., Rammacher, S., Gachot, C., Mücklich, F.: The influence of centrifugal forces on friction and wear in rotational sliding. Tribol. Int. **116**, 256–263 (2017). https://doi.org/10.1016/j.triboint.2017.07.021
30. Gershuni, L., Larson, M.G., Lugt, P.M.: Lubricant replenishment in rolling bearing contacts. Tribol. Trans. **51**(5), 643–651 (2008). https://doi.org/10.1080/10402000802192529
31. Damiens, B., Venner, C.H., Cann, P.M.E., Lubrecht, A.A.: Starved lubrication of elliptical ehd contacts. J. Tribol. **126**(1), 105–111 (2004). https://doi.org/10.1115/1.1631020
32. Greiner, C., Merz, T., Braun, D., Codrignani, A., Magagnato, F.: Optimum dimple diameter for friction reduction with laser surface texturing: the effect of velocity gradient. Surf. Topogr. Metrol. Prop. **3**(4), 044001 (2015). https://doi.org/10.1088/2051-672X/3/4/044001
33. Persson, B.N.J.: Theory of rubber friction and contact mechanics. J. Chem. Phys. **115**(8), 3840–3861 (2001). https://doi.org/10.1063/1.1388626
34. Persson, B.N.J.: Contact mechanics for randomly rough surfaces. Surf. Sci. Rep. **61**(4), 201–227 (2006). https://doi.org/10.1016/j.surfrep.2006.04.001
35. Pradhan, A., Thimons, L.A., Lavrik, N.V., Kravchenko, I.I., Jacobs, T.D.B.: Tuning surface adhesion using grayscale electron-beam lithography. Langmuir **40**(28), 14257–14265 (2024). https://doi.org/10.1021/acs.langmuir.4c00669
36. Hansen, J., Björling, M., Larsson, R.: A new film parameter for rough surface ehl contacts with anisotropic and isotropic structures. Tribol. Lett. **69**(2), 37 (2021). https://doi.org/10.1007/s11249-021-01411-3

Publisher's Note Springer Nature remains neutral with regard to jurisdictional claims in published maps and institutional affiliations.